energy&fuels

Article

pubs.acs.org/EF

Neutron Tomography as a Tool To Study Immiscible Fluids in Porous Media without Chemical Dopants

Julie Murison,[*,†,‡] Robabeh Moosavi,[†] Michael Schulz,[§] Burkhard Schillinger,[§] and Matthias Schröter[*,†]

[†]Max Planck Institute of Dynamics and Self-Organization, 37077 Göttingen, Germany

[‡]Clariant Produkte GmbH, Competence Center Interface and Formulation Technology, 65926 Frankfurt, Germany

[§]FRM II Heinz Maier-Leibnitz Zentrum, Technische Universität München, Garching, Germany

ABSTRACT: We present the first study of fluid distribution inside porous media imaged by neutron tomography. We demonstrate that this technique has matured sufficiently to deliver pore level results. The major advantage of neutron tomography is the contrast mechanism of using deuterated phases. This allows high contrast imaging without the need to add large amounts of inorganic salts as dopants, required to achieve adequate contrast for X-ray tomography studies. Measurements were performed at the Antares beamline (MLZ, Garching) with a voxel size of 11.8 μm. We propose this technique as a useful tool for studying mutliphase phenomena in porous media where the results are known to depend on the salinty and species of ions present, such as low salinity water, surfactant, and polymer flooding.

1. INTRODUCTION

Predicting and controlling multiphase flow in porous media is key to industrial processes such as enhanced oil recovery and CO_2 storage. In particular, it is difficult to predict multiphase flow in natural porous media where the chemical[1] and structural[2,3] complexity of the substrate leads to unknown and varying conditions. Yet evaluation of oil recovery prospects, and potential gas or chemical storage capabilities of geological sites depends crucially on the microstructure and wettability[4,5] of the underlying reservoir.

The global megatrend of increasing energy demands challenges the oil and gas industry to constantly seek new resources and employ enhanced oil recovery techniques. The use of both low, <5000 ppm TDS (total dissolved solids) and high, >35000 ppm TDS, salinity flooding has been shown in certain reservoirs to have positive impacts on oil recovery. Wettability, flow characteristics, and trapping of fluids within reservoir rock depend critically on the constitution of the fluids.[6] In some cases, surfactant and polymers are added to the waterflood in order to overcome unfavorable reservoir wetting conditions and reduce viscous fingering of the water flood. Here again, the performance of the additive depends critically on the salinity of both the formation water and the water used for reservoir flooding.[7−10]

Both at the field scale and in core testing, it has been observed that low salinity water flooding increases the oil output in certain sandstone oil reservoirs.[11−16] A synergistic effect between ionic surfactant flooding and low salinity water has also been observed.[17] In the case of carbonate reservoirs, there are conflicting reports regarding low salinity water. For some carbonate rocks a positive low salinity effect is described.[18] However, for other rock types, flooding with 'Smart water',[19] water with increased concentrations of certain ions, has been used to enhance oil recovery.

There is an increasing body of evidence that the presence of salts can significantly change the properties of the oil/water interface,[20] the behavior of surface active compounds,[21,22] and the wettability of the surface of the porous media.[19,23,24] The direct impact of this on experimental rock-fluid studies is that no results will be independent of the composition of the fluids used. For processes dominated by interfacial tension/capillarity/wettability, it is therefore of utmost importance to measure in systems as close as possible to the natural system of interest.

Due to the economic impacts of these enhanced oil recovery techniques, water/brine composition has become an active area of research. Especially in the case of low salinity flooding, we have some understanding of the underlying mechanisms at the molecular scale.[24−26] However, detailed experimental evidence of the effect of salinity on the flow of oil and the formation of ganglia on the pore-scale is still missing.

Most previous studies of multiphase flow phenomena are based on X-ray tomography. The high flux available in modern synchrotrons allows even dynamic imaging with high spatial resolution.[27] In order to achieve sufficient X-ray contrast between the different phases, it is necessary to use heavy-ion dopants, typically salts such $CsCl_2$, KBr, or ZnI_2 in the aqueous phase. Understanding the mechanisms behind low salinity, and low salinity surfactant water flooding as enhanced oil recovery techniques cannot be readily addressed by X-ray tomography due to the high salt concentrations (>1M) necessary to achieve sufficient X-ray contrast. Confocal microscopy has also been employed to study immiscible flow in quasi-two-dimensional geometries in real time.[28,29] However, this method relies on the use of index-matching liquid phases, strongly restricting the liquid compositions which can be studied.

Here neutron imaging has a significant advantage over X-ray and confocal imaging due to its different contrast mechanism. This is especially true when considering the large difference in the total cross section due to both scattering and absorption

Received: June 24, 2015
Revised: August 24, 2015
Published: August 31, 2015

DOI: 10.1021/acs.energyfuels.5b01403
Energy Fuels 2015, 29, 6271−6276

between the chemically almost identical hydrogen and deuterium: 82.02 barn for hydrogen versus 7.64 barn for deuterium.

Neutron radiography has been successfully employed to visualize single and multiphase flow in porous media.[30−33] Neutron imaging has also been used to visualize the front shape of water moving into sandstones[34] and to make tomography images of sandstones.[35] However, until now, the relatively low spatial resolutions accessible via neutron tomography, around 1.5 mm, have prevented its applications in the field of three-dimensional multiphase imaging and quantitative studies of liquid distributions inside porous media.

Recent advances in scintillator based detection systems in combination with the high neutron flux available at large scale neutron sources have significantly improved the spatial resolution achievable by neutron imaging.[36] At the Antares beamline at the MLZ (Heinz *M*aier-*L*eibnitz *Z*entrum) in Garching, it is now possible to capture tomography images with a voxel size of 11.8 μm. This allows for subpore resolution inside model porous media such as the bead packs used in this study, although measurement times remain comparatively long. However, unlike X-ray imaging, the low energy of thermal neutron beams (4−30 meV) does not result in excessive heating of the sample. Therefore, damage to the fluids, changes in liquid locations, or sample wettability[37] are not expected to occur during imaging.

To this end, we investigated the suitability of neutron tomography as a means of characterizing fluid structures inside porous media. In section 2 we describe the sample preparation, and in section 3 we describe the technical details involved in collecting the tomographies. Section 4 describes the image processing used to extract the different phases from the image, and in section 5 we discuss our experimental results obtained with neutron tomography and compare them with X-ray tomography.

2. EXPERIMENT

Sample Preparation. A sample porous medium was prepared from soda-lime glass beads from Whitehouse scientific with 365 μm mean diameter (measured using the radial distribution function described below). The surfaces of the glass beads were treated by first sputtering a 1 μm thick gold layer on the surface of half of the beads. The thickness of the gold layer was confirmed using AFM for gold sputtered on a glass slide under the same conditions. Then the gold layer was rendered hydrophobic by submerging the beads for 60 min in a 1% volume solution of hexadecanethiol (sigma aldrich) in hexadecane. Beads were then rinsed in isopropanol and dried overnight in the oven. Water in hexadecane contact angles measured on analogously prepared gold coated microscope slides were 120° and on cleaned glass slides were 20°.

As oil phase we used n-hexadecane (Alfa Aesar). Prior to use the hexadecane was filtered through an alumina column to remove any surfactant impurities. The aqueous phase consisted of artificial seawater (henceforth ASW) prepared using the salt concentrations described in reference.[38] ASW was prepared using either Millipore (H_2O), or deuterated (D_2O) water (sigma aldrich) and containing total dissolved solids (TDS) of 35000 ppm. The interfacial tension of both ASW preparations was measured using the pendant drop method on a goniometer (DataPhysics OCA) and found to be 72 ± 1 mN/m against air, and 52 ± 1 mN/m against hexadecane. These results agree with the literature values for the air of 72.74 ± 0.36 mN/m for Millipore water against air[39] and 72.63 ± 0.51 mN/m for D_2O[40] and 54 nM/m for hexadecane system.[2]

Sample containers were made from $AlMg_3$ tubes with an inner diameter of 6 mm and 1 mm wall thickness. Beads were filled into the tube and then stirred through with hexadecane amounting to 30% of the pore volume. To keep this oil phase from redistributing it was frozen at −20° and the remaining interstitial space was filled with artificial seawater in which some air pockets remained in the sample.

Imaging. Neutron tomography was performed in Garching at the Antares beamline at the MLZ of the Technische Universität München. A principle sketch of the beamline and an example image are shown in Figure 1. Tomograms were acquired using 625 projections with an exposure times of either 120 or 240 s per projection using a Gadox (Gadolinium-Oxisulfide) scintillator. Each projection has 2048 by 2048 pixels, at a pixel size of 11.8 μm. Ten open beams were collected before and after imaging in order to correct for the flux density distribution. Including the camera read out time of approximately 10 s, the total imaging time was 24 h for a 120 s exposure time per projection, and 48 h for 240 s exposure time.

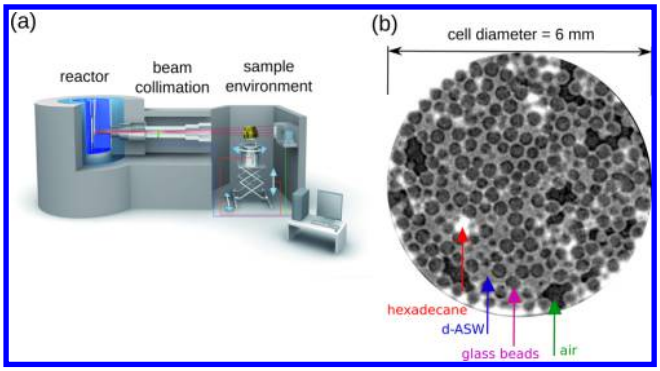

Figure 1. (a) Sketch of the Antares beamline at the MLZ. (b) Cross section of a neutron tomography image using artificial seawater made from D_2O and an exposure time of 240 s per projection. The colored arrows indicate regions of the four different phases.

Figure 1b demonstrates that this experimental protocol provided images with sufficient contrast to distinguish water, oil, air, and beads, using only salt concentrations typically found in seawater, a model system used in core flooding as connate water. In fact, the salt does not contribute to the image contrast. The contrast between the liquid phases is due to the difference in the incoherent scattering length between hydrogen (in the hexadecane) and deuterium (in the deuterated ASW). Consequentially, in this negative image the hexadecane appears the brightest in the sample. The heavy water, having a lower incoherent scattering length, is the middle phase, and the darker areas are comprised of the glass beads and small air inclusions. The gold surface coatings of the beads are not visible by neutron tomography.

The 3D volumes were reconstructed in parallel beam geometry using Octopus, a commercial reconstruction software. One issue arising during neutron tomography is overexposure of single pixels due to single gamma events which originate from the sample and directly hit the camera CCD chip. These pixels can be easily removed by a local median filter which replaces the values of these overexposed pixels with the median value determined from the surrounding pixels. However, this is only possible if the values of the surrounding pixels are correct, that is, not too many pixels have been damaged. In our experiments using 240 s exposure time per projection, only 0.04% of pixels were affected by the gamma events, well below the 10% threshold. These pixels are corrected prior to the reconstruction of the tomography images.

X-ray tomography. After taking the neutron tomographies at the MLZ in Garching, the samples were transported to the MPIDS in Göttingen and X-ray tomographies obtained with a Nanotom (GE Sensing and Inspection), using a tungsten target and 150 kV acceleration voltage. Each tomogram is based on 1400 projections at a scale of 13 μm per voxel. As the transport resulted in minor perturbations of the sample structure, a direct comparison of the bead positions between the two tomographies is not possible.

DOI: 10.1021/acs.energyfuels.5b01403
Energy Fuels 2015, 29, 6271−6276

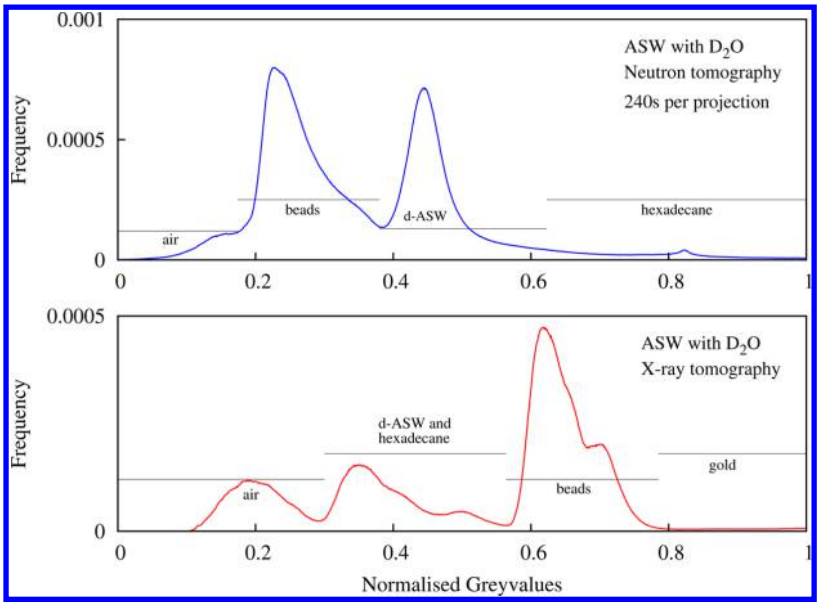

Figure 2. Gray value histogram of both a neutron and a X-ray tomogram, taken after an initial noise removal step using a bilateral filter. For better comparison, all gray value ranges have been normalized from zero to one. The respective ranges of gray values of the different materials are indicated by the horizontal lines.

Image Segmentation. Following reconstruction, the tomograms have to be segmented into the different solid and fluids phases using the gray values of the individual pixels. This process possesses a generic problem for all tomography images due to pixel noise, limited spatial resolution, and limited contrast between the different materials.[41] We performed the segmentation and subsequent analysis with Avizo-Fire, a commercial image processing and analysis software package, using an identical sequence of processing steps for both neutron and X-ray tomographies.

In a first step the image noise was reduced by filtering the reconstructed 3D images using a bilateral filter with a kernel size of 5 × 5 × 5 pixels and 12 iterations. (A bilateral filter is a Gaussian low pass filter which preserves edges by excluding areas of the image which contain high gray value gradients.) Figure 2 displays the resulting gray value histograms of a neutron and a X-ray tomogram.

The different phases are then identified using an iterative protocol: Starting from the low end (black) of the gray value histogram, an appropriate threshold for a phase is manually identified. For the neutron tomogram this corresponds to the air. Pixels corresponding to air have a gray value of less than 0.174. Using this threshold, the image is binarized, and artifacts caused by noise are removed using an opening transformation (successive erosion and dilation steps). The set of voxels corresponding to air are then removed from the image, leaving only a three phase image (water, oil, and beads) for further processing. This process is repeated, taking the next darkest phase until all phases are separated. An example segmentation result is displayed in Figure 3.

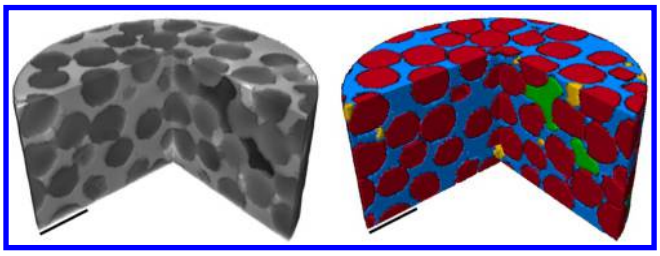

Figure 3. Filtered raw tomogram and segmented neutron tomogram of the sample containing D_2O (blue), hexadecane (yellow), and air (green). Tomography was acquired with an exposure time of 240 s per projection. The scale bars indicated in the images are 500 μm.

In order to evaluate the quality of both the images and multiphase analysis, we calculate the radial distribution function of the glass beads. The individual particle positions of the glass beads cannot be directly obtained, as the spheres overlap at their contact points, creating a continuous network. To separate the beads and obtain the center of mass of each individual sphere, we used the watershed algorithm.

3. RESULTS AND DISCUSSION

Image quality of neutron tomograms. The declared aim of this study is to separate a three fluid system inside a model porous medium into its individual phases. Figure 4 shows four cross sections of tomograms taken under different experimental conditions. The top left panel clearly demonstrates that, using neutron tomography, there is insufficient contrast between H_2O and hexadecane for any kind of reasonable segmentation. The top right cross section corresponds to a neutron tomography using D_2O for the aqueous phase. This significantly improves the contrast between the water and the oil phase. However, the relatively large noise level complicates the segmentation of the liquid features. Therefore, in the bottom left panel the exposure time of each image was doubled. Here all four materials, oil, water, beads, and air, can clearly be distinguished by eye, and segmented for quantitative analysis. The quality of the phase contrast is demonstrated by the histograms in Figure 2 and the segmented views shown in Figure 3. We therefore argue that neutron tomography has matured into a useful tool to study multiphase fluid distributions in porous media.

In this study we have used glass beads with a diameter of 365 μm as a model porous media. It should be noted that bead pack models have a larger porosity (40%) and pore diameter (55 μm)[42] compared to natural reservoir rocks, where porosity can be much lower (10%) and pore sizes may be even submicron.[43] While, at this point in time, neutron tomography would not be able to capture the details of fluid distributions inside very fine grained sandstones or carbonate rocks, the methodology presented in this study and the continually improving scintillator technology will allow for such studies in the future.

DOI: 10.1021/acs.energyfuels.5b01403
Energy Fuels 2015, 29, 6271−6276

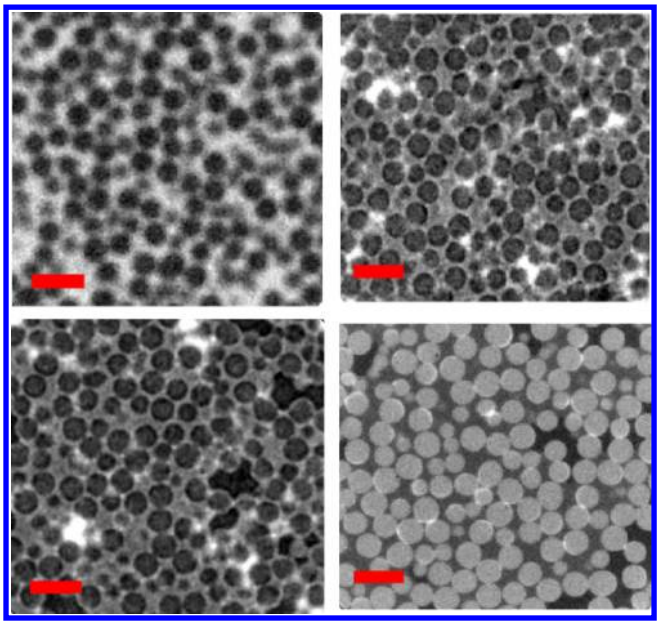

Figure 4. Horizontal cross sections of tomograms. *Top left:* neutron imaging of H_2O/hexadecane (with 1440 min total exposure time), *top right:* D_2O/hexadecane (1440 min, neutron tomography), *bottom left:* D_2O/hexadecane (2880 min, neutron tomography), and *bottom right:* X-ray tomogram of a D_2O/hexadecane system (with 52 min exposure time). The neutron tomography using D_2O/hexadecane/air clearly shows the three different fluid phases, whereas in X-ray tomography the sputtered gold layers are visible. All cross sections are taken at approximately half the sample height. Red scale bars are 1 mm wide.

Comparison between X-ray and neutron imaging. The bottom right panel of Figure 4 shows a cross section of a X-ray tomogram. While the beads and the air can be clearly distinguished, there is no visible contrast between the D_2O and the hexadecane phases. This visual result is supported by the gray value histogram shown in Figure 2, where all potential density differences are smeared out by noise. By comparison, in the neutron tomogram the difference between the mean gray levels of oil and water accounts for approximately 30% of the total dynamic range.

Because the spherical beads can be well segmented for both types of tomographies, they are best suited for a direct comparison of the imaging quality. To this purpose we have computed the radial distribution function which is shown in Figure 5. The radial distribution function describes the probability to find another sphere center at a given distance. The peak at the smallest possible distance corresponds to particles which are directly in contact, which is the most likely configuration in mechanical stable packings. In an ideal, monodisperse packing, the left shoulder of this first peak will be a Heaviside step function. Any deviation from this behavior is either due to slight but unavoidable polydispersity of the beads used in experiments or due to errors in the position detection. As the beads are identical in both experiments, the broadening of the first peak in Figure 5 is indicative of the larger noise level of the neutron tomogram which leads to a reduced precision of the detected particle coordinates. However, while the difference in the peak width is clearly measurable, it is not a strong effect. Additionally, the exact position of the first peak is a very sensitive measure for the average particle diameter,[44] which is here 365 μm.

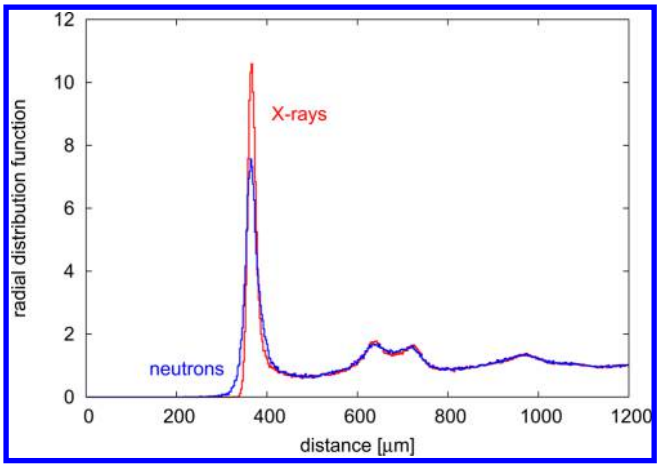

Figure 5. Radial distribution function calculated from the centers of mass of the beads detected in X-rays and neutron tomograms. The first peak corresponds to particles which are in contact. As the particles are sufficiently monodisperse, the width of the first peak is a measure for the precision of the detected particle positions.

The complementary information received from neutron and X-ray tomography highlights the potential for enhanced sample characterization using both techniques on the same, mechanically undisturbed sample. For example, particle positions could be extracted from the X-ray tomogram. The sample voxels corresponding to the beads could be removed from the neutron tomogram during the image preprocessing. This would allow increased accuracy of the boundaries of the oil and water phases. Additionally, the correlation between the positions of the oil droplets and the hydrophobic bead surfaces could be studied, taking advantage of the fact that the gold−thiol surfaces used to hydrophobize the beads are visible in the X-ray tomograms.

4. CONCLUSION

Neutron tomography is a useful tool for studying multiphase systems without the addition of chemical dopants needed for X-ray tomography studies and unlimited by the need for index matched liquids required for confocal microscopy. Using a deuterated aqueous phase provides a strong contrast between oil and water and air. The resolution achieved at the Antares beamline is suitable for further studies of the droplet size distributions and morphologies. Neutron tomography therefore opens a new path for studies where fluid distributions are expected to depend on salt concentrations.

AUTHOR INFORMATION

Corresponding Authors

*E-mail: julie.murison@clariant.com.
*E-mail: matthias.schroeter@ds.mpg.de.

Notes

The authors declare no competing financial interest.

ACKNOWLEDGMENTS

This work is based upon experiments performed at the Antares instrument operated by FRM II at the Heinz Maier-Leibnitz Zentrum (MLZ), Garching, Germany. We gratefully acknowledge BP Plc. for generous funding through the Exploratory Research (ExploRe) program. We thank Wolf Keiderling and Annika von Roden for building the sample chambers and Simon Weis for computing the radial distribution functions.

DOI: 10.1021/acs.energyfuels.5b01403
Energy Fuels 2015, 29, 6271−6276

REFERENCES

(1) Hassenkam, T.; Skovbjerg, L. L.; Stipp, S. L. S. Probing the intrinsically oil-wet surfaces of pores in North Sea chalk at subpore resolution. *Proc. Natl. Acad. Sci. U. S. A.* **2009**, *106* (15), 6071−6076.

(2) Murison, J.; Semin, B.; Baret, J.-C.; Herminghaus, S.; Schröter, M.; Brinkmann, M. Wetting Heterogeneities in Porous Media Control Flow Dissipation. *Phys. Rev. Appl.* **2014**, *2*, 034002.

(3) Herminghaus, S. Universal Phase Diagram for Wetting on Mesoscale Roughness. *Phys. Rev. Lett.* **2012**, *109*, 236102.

(4) Anderson, W. Wettability Literature Survey- Part 4: Effects of Wettability on Capillary Pressure. *JPT, J. Pet. Technol.* **1987**, *39*, 1283−1300.

(5) Morrow, N. R. Wettability and Its Effect on Oil Recovery. *JPT, J. Pet. Technol.* **1990**, *42*, 1477−1484.

(6) Muhammad, Z. Compositional Dependence of Reservoir Wettability. *SPE International Symposium on Oil field Chemistry* **2001**, DOI: 10.2118/65409-MS.

(7) Alagic, E.; Skauge, A. Combined Low Salinity Brine Injection and Surfactant Flooding in Mixed-Wet Sandstone Cores. *Energy Fuels* **2010**, *24*, 3551−3559.

(8) Alagic, E.; Spildo, K.; Skauge, A.; Solbakken, J. Effect of crude oil ageing on low salinity and low salinity surfactant flooding. *J. Pet. Sci. Eng.* **2011**, *78*, 220−227.

(9) Shiran, B. S.; Skauge, A. Enhanced Oil Recovery (EOR) by Combined Low Salinity Water-Polymer Injection. *Energy Fuels* **2013**, *27*, 1223.

(10) Shiran, B. S.; Skaugea, A. Similarities and Differences of Low Salinity Polymer and Low Salinity LPS (Linked Polymer Solutions) for Enhanced Oil Recovery. *J. Dispersion Sci. Technol.* **2014**, 35.165610.1080/01932691.2013.879532

(11) Tang, G. Q.; Morrow, N. R. Effect of temperature, salinity and oil composition on wetting behavior and oil recovery by waterflooding. *SPE annual technical conference and exhibition: Denver CO* **1996**, 6−9.

(12) Tang, G.-Q.; Morrow, N. R. Influence of brine composition and fines migration on crude oil/brine/rock interactions and oil recovery. *J. Pet. Sci. Eng.* **1999**, *24*, 99−111.

(13) Webb, K. J.; Black, C. J. J.; Edmonds, I. J. Low Salinity Oil Recovery - The Role of Reservoir Condition Corefloods. *13th European Symposium on Improved Oil Recovery Budapest Hungary*, 2005.

(14) Zhang, P.; Tweheyo, M. T.; Austad, T. Wettability alteration and improved oil recovery by spontaneous imbibition of seawater into chalk: Impact of the potential determining ions Ca^{2+}, Mg^{2+}, and SO_4^{2-}. *Colloids Surf., A* **2007**, *301*, 199−208.

(15) Sorbie, K. E.; Collins, I. R. A Proposed Pore-Scale Mechanism for How Low Salinity Waterflooding Works. *SPE Improved Oil Recovery Symposium in Tulsa, Oklahoma*, **2010**, SPE 129833. DOI: 10.2118/129833-MS.

(16) Austad, T.; Shariatpanahi, S. F.; Strand, S.; Black, C. J. J.; Webb, K. J. Conditions for a Low-Salinity Enhanced Oil Recovery (EOR) Effect in Carbonate Oil Reservoirs. *Energy Fuels* **2012**, *26*, 569−575.

(17) Alagic, E.; Skauge, A. Combined Low Salinity Brine Injection and Surfactant Flooding in Mixed-Wet Sandstone Cores. *Energy Fuels* **2010**, *24*, 3551−3559.

(18) Mahani, H.; Keya, A. L.; Berg, S.; Bartels, W.; Nasralla, R.; Rossen, W. R. Insights into the Mechanism of Wettability Alteration by Low-Salinity-Flooding (LSF) in Carbonates. *Energy Fuels* **2015**, *29*, 1352−1367.

(19) Strand, S.; Austad, T.; Puntervold, T.; Høgnesen, E. J.; Olsen, M.; Barstad, S. M. F. Smart Water" for Oil Recovery from Fractured Limestone: A Preliminary Study. *Energy Fuels* **2008**, *22*, 3126−3133.

(20) Alvarez, G.; Jestin, J.; Argillier, J. F.; Langevin, D. Small-Angle Neutron Scattering Study of Crude Oil Emulsions: Structure of the Oil-Water Interfaces. *Langmuir* **2009**, *25*, 3985−3990.

(21) Jensen, G. V.; Lund, R.; Gummel, J.; Narayanan, T.; Pedersen, J. S. Monitoring the Transition from Spherical to Polymer-like Surfactant Micelles Using Small-Angle X-Ray Scattering. *Angew. Chem., Int. Ed.* **2014**, *53*, 11524−11528.

(22) Eckold, G.; Gorski, N. Small-angle neutron scattering from tetradecyltrimethylammonium bromide in NaBr aqueous solutions. *Colloids Surf., A* **2001**, *183−185*, 361−369.

(23) Hassenkam, T.; Pedersen, C. S.; Dalby, K.; Austad, T.; Stipp, S. L. S. Pore scale observation of low salinity effects on outcrop and oil reservoir sandstone. *Colloids Surf., A* **2011**, *390*, 179−188.

(24) Hassenkam, T.; Mitchell, A. C.; Pedersen, C. S.; Skovbjerg, L. L.; Bovet, N.; Stipp, S. L. S. The low salinity effect observed on sandstone model surfaces. *Colloids Surf., A* **2012**, *403*, 79−86.

(25) Matthiesen, J.; Bovet, N.; Hilner, E.; Andersson, M. P.; Schmidt, D. A.; Webb, K. J.; Dalby, K. N.; Hassenkam, T.; Crouch, J.; Collins, I. R.; Stipp, S. L. S. How Naturally Adsorbed Material on Minerals Affects Low Salinity Enhanced Oil Recovery. *Energy Fuels* **2014**, *28*, 4849−4858.

(26) Siretanu, I.; Ebeling, D.; Andersson, M. P.; Stipp, S. L. S.; Philipse, A.; Stuart, M. C.; van den Ende, D.; Mugele, F. Direct observation of ionic structure at solid-liquid interfaces: a deep look into the Stern Layer. *Sci. Rep.* **2014**, *4*, 4956.

(27) Berg, S.; Ott, H.; Klapp, S. A.; Schwing, A.; Neiteler, R.; Brussee, N.; Makurat, A.; Leu, L.; Enzmann, F.; Schwarz, J.-O.; Kersten, M.; Irvine, S.; Stampanoni, M. Real-time 3D imaging of Haines jumps in porous media flow. *Proc. Natl. Acad. Sci. U. S. A.* **2013**, *110*, 3755−3759.

(28) Datta, S. S.; Chiang, H.; Ramakrishnan, T. S.; Weitz, D. A. Spatial Fluctuations of Fluid Velocities in Flow through a Three-Dimensional Porous Medium. *Phys. Rev. Lett.* **2013**, *111*, 064501.

(29) Krummel, A. T.; Datta, S. S.; Münster, S.; Weitz, D. A. Visualizing multiphase flow and trapped fluid configurations in a model three-dimensional porous medium. *AIChE J.* **2013**, *59*, 1022−1029.

(30) Jasti, J. K.; Fogler, H. S. Application of Neutron Radiography to Image Flow Phenomena in Porous Media. *AIChE J.* **1992**, *38*, 481−488.

(31) Shokri, N.; Lehmann, P.; Or, D. Evaporation from layered porous media. *J. Geophys. Res.* **2010**, *115*, B06204.

(32) Masschaele, B.; Dierick, M.; Cnudde, V.; van Hoorebeke, L.; Delputte, S.; Gildemeister, A.; Gaehler, R.; Hillenbach, A. High-speed thermal neutron tomography for the visualization of water repellents, consolidants and water uptake in sand and lime stones. *Radiat. Phys. Chem.* **2004**, *71*, 807−808.

(33) de Beer, F. C.; Middleton, M. F. Neutron radiography imaging, porosity and permeability in porous rocks. *S. Afr. J. Geol.* **2006**, *109*, 541−550.

(34) Dierick, M.; Vlassenbroeck, J.; Masschaele, B.; Cnudde, V.; van Hoorebeke, L.; Hillenbach, A. High-speed neutron tomography of dynamic processes. *Nucl. Instrum. Methods Phys. Res., Sect. A* **2005**, *542*, 296−301.

(35) Solymar, M.; Lehmann, E.; Vontobel, P.; Nordlund, A. Relating variations in water saturation of a sandstone sample to pore geometry by neutron tomography and image analysis of thin sections. *Bull. Eng. Geol. Environ.* **2003**, *62*, 85−88.

(36) Hess, K.-U.; Flaws, A.; Mühlbauer, M. J.; Schillinger, B.; Franz, A.; Schulz, M.; Calzada, E.; Dingwell, D. B.; Bente, K. Advances in high-resolution neutron computed tomography: Adapted to the earth sciences. *Geosphere* **2011**, *7*, 1294−1302.

(37) Brown, K.; Schlüter, S.; Sheppard, A.; Wildenschild, D. On the challenges of measuring interfacial characteristics of three-phase fluid flow with x-ray microtomography. *J. Microsc.* **2014**, *253*, 171−182.

(38) Kester, D. R.; Duedall, I. W.; Connors, D. N.; Pytkowicz, R. M. Preparation of Artificial Seawater. *Limnol. Oceanogr.* **1967**, *12*, 176−179.

(39) Cooper, J.; Dooley, R. B. *IAPWS Release on surface tension of ordinary water substance* **1994**, 1−6.

(40) Cooper, J.; Dooley, R. B. *IAPWS Release on surface tension of heavy water substance* **1994**, 1−5.

(41) Wildenschild, D.; Sheppard, A. P. X-ray imaging and analysis techniques for quantifying pore-scale structure and processes in subsurface porous medium systems. *Adv. Water Resour.* **2013**, *51*, 217−246.

DOI: 10.1021/acs.energyfuels.5b01403
Energy Fuels 2015, 29, 6271−6276

(42) McGEARY, R. K. Mechanical Packing of Spherical Particles. *J. Am. Ceram. Soc.* **1961**, *44*, 513−522.
(43) Nelson, P. Pore-throat sizes in sandstones, tight sandstones, and shales. *AAPG Bull.* **2009**, *93*, 329−340.
(44) Finger, T.; Schröter, M.; Stannarius, R. The mechanism of pattern coarsening in rotating drums. *arXiv:1412.7459 [cond-mat]*, 2015.

DOI: 10.1021/acs.energyfuels.5b01403
Energy Fuels 2015, 29, 6271−6276